AGU PUBLICATIONS

Geophysical Research Letters

RESEARCH LETTER

10.1002/2016GL069799

Key Points:

- Persistent artifacts have been found in the NSIDC data set
- These artifacts significantly impact calculation of sea ice motion gradients
- These artifacts lead to significant underestimation of MYI extent

Supporting Information:

- Supporting Information S1
- Movie S1

Correspondence to:
S. Szanyi,
szanyis@ethz.ch

Citation:
Szanyi, S., J. V. Lukovich, D. G. Barber, and G. Haller (2016), Persistent artifacts in the NSIDC ice motion data set and their implications for analysis, *Geophys. Res. Lett.*, *43*, 10,800–10,807, doi:10.1002/2016GL069799.

Received 28 MAY 2016
Accepted 29 SEP 2016
Accepted article online 4 OCT 2016
Published online 24 OCT 2016

Persistent artifacts in the NSIDC ice motion data set and their implications for analysis

S. Szanyi[1], J. V. Lukovich[2], D. G. Barber[2], and G. Haller[1]

[1]Institute for Mechanical Systems, ETH Zürich, Zürich, Switzerland, [2]Centre for Earth Observation Science, Faculty of Environment, Earth, and Resources, University of Manitoba, Winnipeg, Manitoba, Canada

Abstract In this study we evaluate weekly Equal-Area Scalable Earth Grid (EASE-Grid) sea ice velocities released by the National Snow and Ice Data Centre (NSIDC). We identify persistent Eulerian and Lagrangian features that arise solely as an artifact of the method used in the incorporation of buoy data. This, in turn, significantly impacts calculation of sea ice motion gradients, including divergence, convergence, and shear. Our numerical experiments and comparison with observations further demonstrate the impact of these artificial features on climatological assessments, including age-of-ice studies. In particular, we find that age-of-ice studies using this data set significantly underestimate multiyear ice extent by an average of 0.8×10^6 km^2 in the month of March.

1. Introduction

Sea ice plays a unique and important role in the Arctic climate system. Sea ice dynamics, namely, drift and deformation, provide information on atmosphere-ocean momentum and heat exchange associated with polynya and lead formation, with implications for contaminant transport and thickness redistribution [*Rampal et al.*, 2009; *Spreen et al.*, 2011; *Hutchings and Rigor*, 2012; *Marcq and Weiss*, 2012; *Eicken and Mahoney*, 2015]. Studies related to sea ice drift and deformation also provide the insight required for improved representation of physics in sea ice-ocean models [*Bouillon and Rampal*, 2015], which is relevant for ice hazard detection and forecasting. Sea ice dynamics studies use both Eulerian data, such as satellite-derived ice motion [e.g., *Maslanik et al.*, 2011] and Lagrangian data, such as buoy trajectories [e.g., *Rampal et al.*, 2009; *Hutchings et al.*, 2011]. Only the former class provides, however, uniform spatial and temporal coverage of sea ice motion. This aids the understanding of simultaneous large-scale changes in sea ice drift and ice deformation in response to a changing climate.

A recent study by *Sumata et al.* [2014] compared, and provided uncertainty estimates for, all publicly available satellite-derived sea ice drift products: Ocean and Sea Ice Satellite Application Facility (OSI SAF), National Snow and Ice Data Centre (NSIDC), Centre ERS d'Archivage et de Traitement (CERSAT), and sea ice drift data from *Kimura et al.* [2013]. The conclusion was that spatial and temporal uncertainty in all ice drift products depends on the (i) satellite data used as input, (ii) ice-tracking algorithm, (iii) interpolation techniques, and (iv) spatial and temporal scales evaluated. In an assessment of uncertainty in monthly Arctic sea ice drift, using empirical error and bias functions, recent studies showed that the error depended on ice drift speed and/or ice concentration and differed between ice drift products [*Sumata et al.*, 2015a, 2015b]. Uncertainty in NSIDC sea ice drift fields in winter, in particular, exhibited a systematic error or bias and was found to be dependent on ice drift speed and concentration [*Sumata et al.*, 2015b].

Of all publicly available ice drift products, NSIDC provides the longest temporal and the finest spatial coverage of sea ice drift data. Furthermore, this product is the only one that is available over decades and, therefore, appropriate for climatological assessments. Based on this data set, ice age and thickness studies have documented the transition from a multiyear ice (MYI) to a first-year ice (FYI) regime in recent years, with implications for summertime sea ice extent [*Rigor and Wallace*, 2004; *Fowler et al.*, 2003; *Maslanik et al.*, 2007; *Tschudi et al.*, 2010; *Stroeve et al.*, 2011; *Maslanik et al.*, 2011]. Central to each of these analyses is the advection of particles in a sequence of Eulerian ice drift fields and the monitoring/analysis of forward-time trajectories associated with evolution in the ice drift field.

Also of interest is evolution in spatial gradients in the ice drift field, namely, shear- and divergence-dominated fields associated with ridging, rafting, and polynya formation. The realistic representation of evolution in differential fields with minimal uncertainty will be essential in providing an accurate representation of sea ice deformation and transport characteristics of sea ice on regional and smaller scales in ice-ocean models. Furthermore, accurate characterization of the spatiotemporal evolution in sea ice motion gradients will be relevant for identifying regions associated with heat and moisture exchange due to fracturing in the ice cover.

The initial objective of this study was to identify persistent features in the deformation field by applying Eulerian and Lagrangian indicators to the NSIDC sea ice drift data set. This objective had to be modified, because Eulerian and Lagrangian diagnostics have turned out to show persistent features due to a systematic error arising from the way satellite and buoy data is merged. We identify the source of this error using Eulerian and Lagrangian metrics. We also assess the impact of this error on previous Lagrangian studies, providing climatological assessments and age-of-ice estimates.

2. Data: NSIDC Sea Ice Motion Gridded Data

In this study the National Snow and Ice Data Centre (NSIDC) "Polar Pathfinder Daily 25 km EASE-GRID Sea Ice Motion Vectors, Version 3" data set is evaluated. NSIDC daily ice motion vectors are computed from an algorithm that performs optimal interpolation using several data sources. These sources range from passive microwave radiometers, such as the Scanning Multichannel Microwave Radiometer (SMMR) to International Arctic Buoy Programme (IABP) buoy data. Daily gridded fields combine data from all sensors, from November 1978 to May 2015 [*Tschudi et al.*, 2016]. This is currently the only available product that combines buoy and satellite measurements. We use weekly data for consistency with other applications and studies using the weekly NSIDC sea ice motion data set.

3. Methods

In order to identify persistent features in the ice drift field, we use Eulerian and Lagrangian diagnostics that quantify the stretching and compressibility present in the sea ice deformation and fracturing process. Weekly data are used for Eulerian metrics, and weekly data integrated over 1 year are used for Lagrangian metrics.

3.1. Eulerian Metrics

From the zonal and meridional components v_x and v_y of the two-dimensional ice velocity field $\mathbf{v}(\mathbf{x}, t) = (v_x(\mathbf{x}, t), v_y(\mathbf{x}, t))$, the ice drift speed $V(\mathbf{x}, t)$ is obtained as

$$V(\mathbf{x}, t) = \sqrt{v_x^2(\mathbf{x}, t) + v_y^2(\mathbf{x}, t)}\,. \tag{1}$$

We first examine objective (frame independent) ice drift speed patterns to highlight ice motion features from an Eulerian perspective. The larger eigenvalue ($\Lambda[\dot{\epsilon}]$) of the Eulerian rate-of-strain tensor

$$\dot{\epsilon}(\mathbf{x}, t) = \frac{1}{2}\left[\nabla\mathbf{v}(\mathbf{x}, t) + \nabla\mathbf{v}^{\top}(\mathbf{x}, t)\right], \tag{2}$$

provides such an objective assessment of stretching, while the sea ice divergence

$$D(\mathbf{x}, t) = \nabla \cdot \mathbf{v}(\mathbf{x}, t)\ , \tag{3}$$

provides an objective measure of compressibility (ice cover opening and closing) in the ice drift field. We compute spatial gradients at the resolution of the NSIDC EASE-Grid data set (25 km).

3.2. Lagrangian Metrics

Here we introduce Lagrangian counterparts of the above Eulerian metrics. First, we consider a two-dimensional, unsteady velocity field $\mathbf{v}(\mathbf{x}, t)$, with the time t defined over a finite interval $[t_0, t_1]$. In this velocity field, all trajectories satisfy the following ordinary differential equation:

$$\dot{\mathbf{x}} = \mathbf{v}(\mathbf{x}, t)\ . \tag{4}$$

Let $\mathbf{x}\left(t; t_0, \mathbf{x}_0\right)$ denote the time t position of the ice trajectory starting from $\mathbf{x}_0$ at time t_0. We track particles by solving the equation of motion (4) with a variable step, fourth and fifth-order Runge-Kutta (also known as Dormand-Prince) scheme, using bilinear spatial interpolation, and initial conditions $\mathbf{x}_0 = \mathbf{x}\left(t_0\right)$ set up on an equally spaced grid. We will plot various Lagrangian scalar fields over initial conditions of particles that did not reach the boundary and survived the melt season.

3.2.1. Finite-Time Lyapunov Exponent

Finite-Time Lyapunov Exponents (FTLEs) are used to provide a Lagrangian interpretation of stretching in the ice drift field. We define the flow (advection) map between the initial time t_0 and elapsed time T as

$$\mathbf{F}_{t_0}^{t_0+T}\left(\mathbf{x}_0\right) = \mathbf{x}\left(t; t_0, \mathbf{x}_0\right) \ , \tag{5}$$

and the right Cauchy-Green strain tensor as

$$\mathbf{C}_{t_0}^{t_0+T}\left(\mathbf{x}_0\right) = \left(\nabla \mathbf{F}_{t_0}^{t_0+T}\left(\mathbf{x}_0\right)\right)^{\top} \nabla \mathbf{F}_{t_0}^{t_0+T}\left(\mathbf{x}_0\right), \tag{6}$$

with the superscript $^{\top}$ referring to matrix transposition. The finite-time Lyapunov exponent for the trajectory $\mathbf{x}\left(t; t_0, \mathbf{x}_0\right)$ is defined from the largest eigenvalue $\lambda_{\max}\left[\mathbf{C}_{t_0}^{t_0+T}\left(\mathbf{x}_0\right)\right]$ of the right Cauchy-Green strain tensor [*Haller*, 2001, 2015]. Since $\sqrt{\lambda_{\max}}$ gives the magnitude of the largest stretching, the FTLE is defined as

$$\Lambda_{t_0}^{t_0+T}(\mathbf{x}_0) = \frac{1}{|T|} \log \sqrt{\lambda_{\max}\left[\mathbf{C}_{t_0}^{t_0+T}(\mathbf{x}_0)\right]}. \tag{7}$$

Positive FTLEs capture exponential stretching, while negative FTLEs capture contraction possible only in compressible (divergent) flow. Maximum curves in the FTLE field, known as ridges, mark material lines of maximal stretching. By monitoring the rate of trajectory separation, FTLEs reveal large-scale and long-term persistent features in the sea ice deformation field that are relevant for dispersion studies, including pollutant and contaminant transport.

3.2.2. Lagrangian-Averaged Divergence

In order to measure Lagrangian features arising from the compressible nature of the deformation, we introduce the Lagrangian-averaged divergence (LAD) as

$$\mathrm{LAD}_{t_0}^{t_0+T}\left(\mathbf{x}_0\right) = \frac{1}{|T|}\left[\int_{t_0}^{t_0+T} \mathrm{div}\mathbf{v}\left(\mathbf{F}_{t_0}^{t_0+T}\left(\mathbf{x}_0\right), t\right) \mathrm{d}t\right]. \tag{8}$$

By Liouville's theorem [*Arnold*, 1978], we have

$$\begin{aligned} \mathrm{LAD}_{t_0}^{t_0+T}(\mathbf{x}_0) &= \frac{1}{|T|} \log\left(\det \nabla \mathbf{F}_{t_0}^{t_0+T}\left(\mathbf{x}_0\right)\right) \\ &= \frac{1}{2|T|} \log\left(\det \nabla \mathbf{C}_{t_0}^{t_0+T}\left(\mathbf{x}_0\right)\right) \\ &= \frac{1}{2|T|} \log \lambda_{\min}\left(\mathbf{x}_0\right) + \Lambda_{t_0}^{t_0+T}\left(\mathbf{x}_0\right) \ , \end{aligned} \tag{9}$$

where $\lambda_{\min}\left(\mathbf{x}_0\right)$ denotes the smaller eigenvalue of the Cauchy-Green strain tensor. According to (8), LAD is directly computable from the eigenvalues of $\mathbf{C}_{t_0}^{t_0+T}\left(\mathbf{x_0}\right)$.

4. Results and Discussion

4.1. Evaluation of the Data Set

Evaluation of the objective Eulerian (using weekly data) and Lagrangian (using a 1 year integration time) diagnostics described in section 3 for the NSIDC data set reveals persistent circular structures (Figure 1). In order to explain these features, we recall the data processing technique for the NSIDC sea ice drift data product. The ice motion estimates from each sensor (satellite, wind, and buoy observations) are computed and gridded individually. The previously generated independent estimates are then merged into a final motion estimate using a source-weighted and distance-weighted average of the nearest 15 estimates. Since buoys are considered the most accurate sensors, they receive the highest weighting in the interpolation process. However, as opposed to other sensors, buoys only record the positions of a single ice floe, which may not be representative of ice drift on larger scales (100 km). Therefore, the velocity field is split into buoy-affected and background regions.

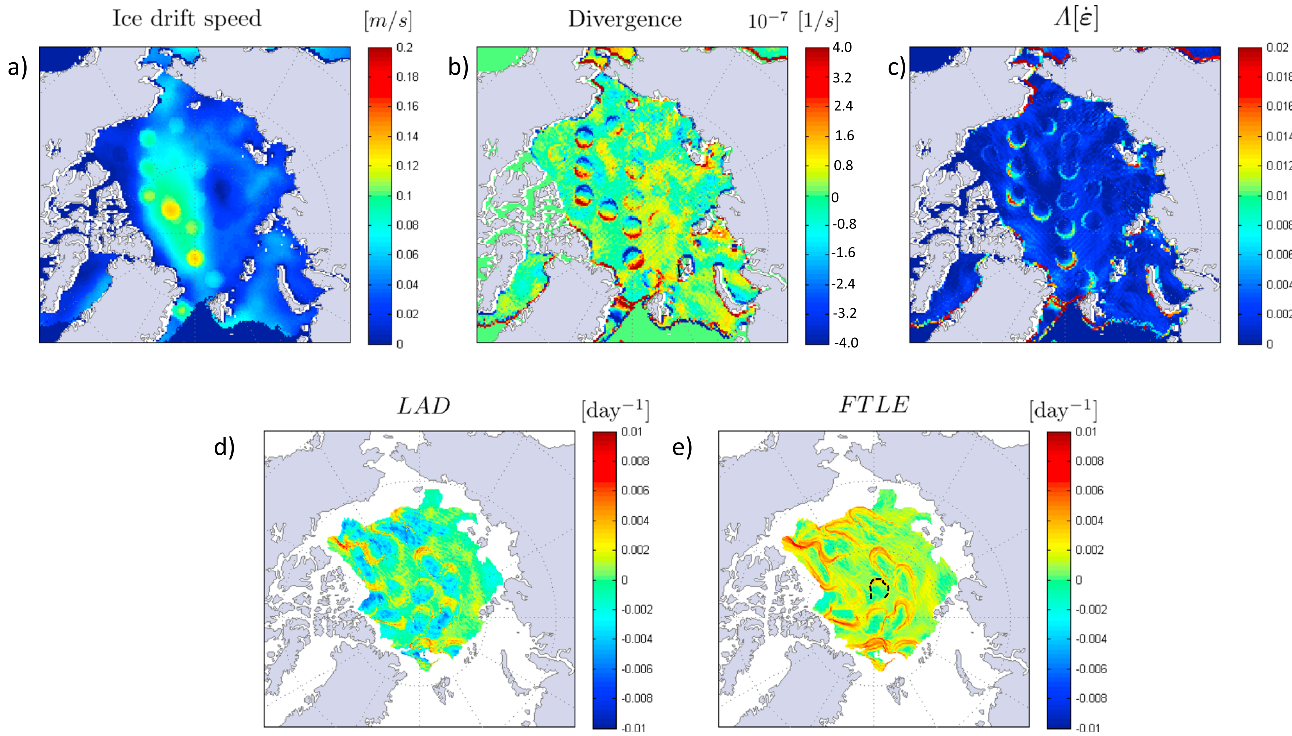

Figure 1. Eulerian indicator maps for week 11 in 1979, namely, (a) ice drift speed, (b) divergence, (c) larger eigenvalue of the Eulerian strain rate tensor. Lagrangian indicator maps integrated between 1 January 1979 and 1 January 1980, namely, (d) LAD and (e) FTLE (where a horseshoe-shaped ridge is highlighted by a black dashed line).

Previous studies already observed that buoys report higher velocities than satellites, with differences on the order of several centimeters per second [*Schwegmann et al.*, 2011]. This difference creates sharp circular features in the ice drift speed fields (Figure 1a), centered at buoy locations. In the Eulerian divergence field, these circular features suggest strong convergence in the direction of buoy motion and strong divergence in the opposite direction, due to the higher buoy speed relative to the background field (Figure 1b; for 2014 see Movie S1 in the supporting information). The same circular features appear as significant stretching patterns in the $\Lambda[\dot{\varepsilon}]$-field (Figure 1c).

Artificial convergence cores arise in the Lagrangian-averaged divergence (Figure 1d), displaying filaments with large LAD values at the periphery of the buoy-affected regions. In the finite-time Lyapunov exponent (FTLE) field (Figure 1e), horseshoe-shaped ridges arise in the same locations. These ridges can be found every year between 1979 and 2015. These horseshoe-shaped stretching ridges show insensitivity to noise in the order of 1–2 cm/s. We have recovered these patterns in every year of the data set, which highlights the inapplicability of this product for any Eulerian or Lagrangian analysis requiring differentiation or spatial gradients.

To ascertain that buoys are responsible for these features, we have performed a comparative studies on the Ocean and Sea Ice Satellite Application Facility (OSI SAF) [*Lavergne et al.*, 2010] low-resolution ice motion data set. Out of all publicly available data sets, OSI SAF exhibits the highest level of correlation with NSIDC [*Sumata et al.*, 2014]. In particular, scatter plots of monthly ice drift speeds for NSIDC versus OSI SAF showed correlations of $r \approx 0.96$ [*Sumata et al.*, 2014, Figure 10], while the mean and standard deviation ice drift difference in high-concentration regimes was lowest for both NSIDC and OSI SAF data. Interestingly, recent studies found the NSIDC data set to perform comparably to OSI SAF when uncertainties were evaluated based on buoy trajectories [*Sumata et al.*, 2014]. However, when uncertainty was evaluated based on Synthetic Aperture Radar (SAR) data, NSIDC strongly underperformed relative to OSI SAF [*Sumata et al.*, 2015b]. We have found that diagnostic maps based on OSI SAF do not show artificial structures (see Supporting Information S1 for details). This comparison confirms that the artificial circular features produced by NSIDC in objective diagnostic fields

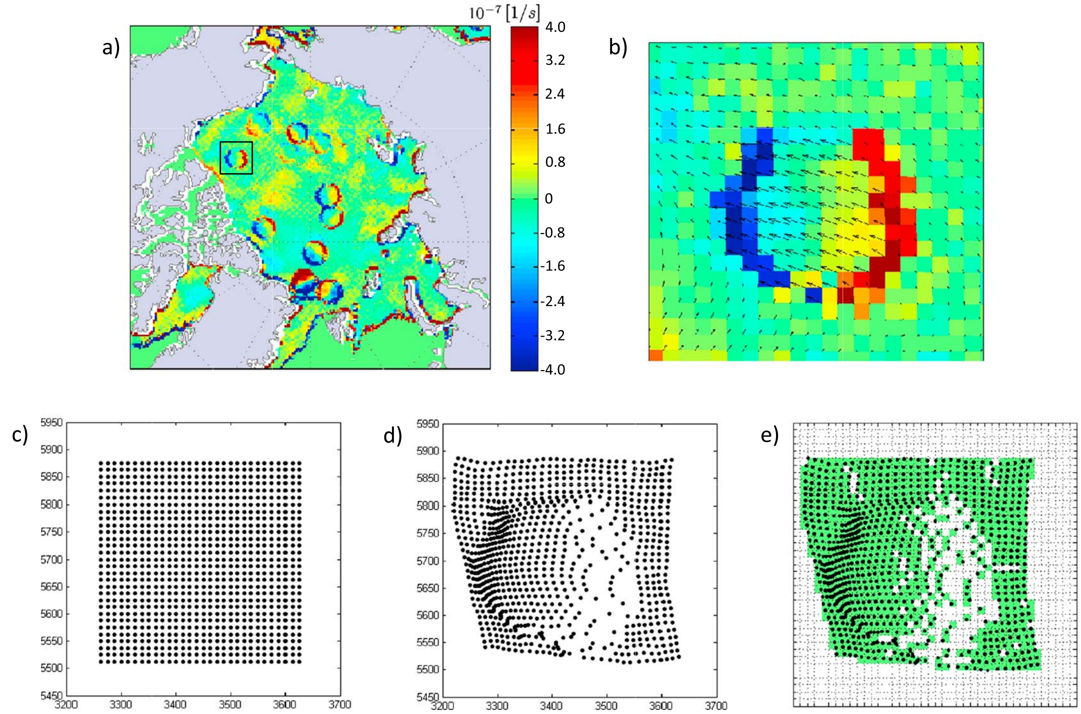

Figure 2. Numerical experiment highlighting the implications of buoy-affected regions for age-of-ice calculations. (a) Eulerian divergence field for week 10 in 1979. (b) Steady velocity field of the investigated buoy-affected region. (c) Initial and (d) final positions of the particles. (e) Evaluation of the final positions, with cells that were occupied by a particle colored green. Noteworthy is the emergence of gaps resulting from artificial divergence in buoy-affected regions.

are solely the result of a direct inclusion of buoy velocities in a velocity field that is characteristic of larger-scale ice motion. It should be noted that we observed similar features in earlier versions of the NSIDC data set.

4.2. Implications for Age-of-Ice Studies

Several age-of-ice and ice thickness studies using the NSIDC data set have been published in the last decade [*Maslanik et al.*, 2007; *Stroeve et al.*, 2011; *Maslanik et al.*, 2011]. In these studies, ice age is calculated by advecting each grid cell as a Lagrangian parcel on weekly time steps using the NSIDC velocity data. Provided the grid cell/parcel survives the summer melt season and sustains ice concentrations exceeding 15%, the age category at each cell is incremented by 1 year. The resulting sea ice age maps for the integrated time frame capture sea ice extent and regions defined by different ice ages. Multiyear ice (MYI) extent is defined based on parcels that have survived at least one melt season, whereas first-year ice (FYI) extent is defined based on those parcels that have not yet survived a melt season.

To assess the impact of artificially generated divergence on age-of-ice calculations, we have performed a numerical experiment. We have focused on one buoy-affected region, and its vicinity, using a weekly drift field from 1979 March (Figures 2a and 2b). An initial configuration of 900 particles located in that region (Figure 2c) is advected for 8 weeks (Figure 2d) in a steady velocity field (Figure 2b), which was chosen for simplicity. Initially, each particle occupies a grid cell. After 8 weeks, only 711 grid cells are occupied by a particle (Figures 2d and 2e), indicating approximately 20% loss of MYI extent due to the discontinuity and artificial divergence in the buoy-affected region. About 2% loss in MYI ice extent happened to be in the background field (evident in white patches within green background in Figure 2e), due to compressibility.

The traditional age-of-ice calculation method [*Fowler et al.*, 2003; *Maslanik et al.*, 2007] launches exactly the number of particles that covers the area in an equidistant manner; if the flow is incompressible (area preserving), the same area would be occupied by the particles independent of the integration length. Since the ice drift field is compressible, not all grid cells will be occupied. As a consequence the current age-of-ice method will always underestimate the sea ice extent, even if one uses a perfect data set without any artificial divergence. In order to provide a more realistic representation of the large number of floes with sizes less than

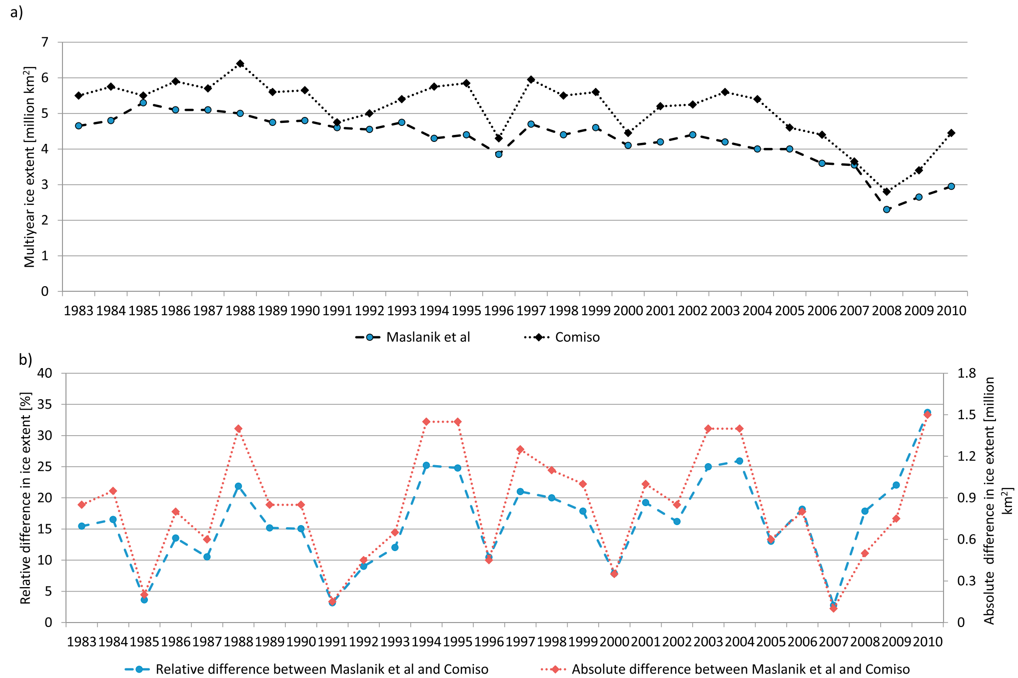

Figure 3. (a) Multiyear ice extent based on *Maslanik et al.* [2011] and *Comiso* [2012]; (b) Relative and absolute difference between the two results.

the evaluation grid spacing, we have advected a denser grid of initial conditions than the evaluation grid. This advection scheme reduces artificial loss of ice extent. We tested this modification using an 8 km initial grid and a 25 km evaluation grid on the time-varying OSI SAF data. We have found the loss in the ice extent map after 6 months to be less than 1%. In a more complicated unsteady case, the artificial divergence creates large LAD convergence cores as shown in Figure 1d. Overall, the majority of the sea ice extent loss results from the artificial divergence, creating a "tear" or "holes" in the ice drift fabric.

In order to assess the cumulative impact of these artificial features over several decades, it is necessary to compare the results of the model associated with ice age studies with independent measurements. Ice age studies define Multiyear Ice (MYI) as the set of ice parcels that survive at least one summer melt cycle [*Maslanik et al.*, 2007, 2011]. In *Comiso* [2012] and *Comiso and Hall* [2014], perennial ice is defined as ice that survives at least one summer season and is associated with the September minimum in sea ice extent. These authors define MYI as the thick component of perennial ice. In these studies MYI is derived from passive microwave data in winter based on a strong contrast in passive microwave signatures for FYI and MYI due to differences in salinity (between 10 and 12 psu for FYI and about 0 psu for MYI), and a 30% ice concentration threshold to exclude second-year ice types [*Comiso*, 2012].

In order to assess the impact of artificial divergence features in buoy-affected areas of ice age and thickness estimates, we compare MYI extent in March determined from observations in *Comiso* [2012] from 1983 to 2010 (Figure 3) with the ice age results of *Maslanik et al.* [2011]. We find that sea ice extent obtained from the NSIDC drift field consistently underestimates the measured sea ice extent (Figure 3a). The absolute difference varies between 0.1 and 1.5×10^6 km^2 with an average of 0.8×10^6 km^2. Relative difference graphs show that the underestimation in March ranges from less than 5% to 35% (Figure 3b). Possible sources for this discrepancy include uncertainties associated with observations. A comparatively small $0.07{\times}10^6$ km^2 bias is noted in observations and satellite-derived sea ice extent [*Comiso*, 2012], which therefore cannot account for the difference. Furthermore, we set up a numerical experiment in which Maslanik's MYI definition is used so that every particle which survives one melt season is MYI. From this definition, it follows that after the yearly ice extent minimum in September each ice parcel is MYI; therefore, the satellite measured ice extent should be the same as the modeled MYI extent. However, by comparison, we find large holes in the model which filled with MYI in the measurements. The cumulative area of the holes is comparable with the difference between Comiso's observations and Maslanik's results. Only the artificial divergence can create holes in the modeled September ice extent; therefore, measurement errors which do not cause artificial divergence cannot be the reason for the difference. We also see in the Lagrangian and the Eulerian metrics that the artificial divergence due to merging buoy and satellite data is 1–2 orders of magnitude larger than the background divergence (the background divergence can be split into real physical divergence and measurement errors). Therefore, we conclude that the major source of the difference between Comiso's measurement and Maslanik's results is the artificial divergence caused by including buoy data using MCC and cokriging methods.

One of the main results of age-of-ice studies is the distribution of ice age as a signature of thickness distributions. Due to the artificial divergence described here, those thickness results are inconclusive. They underestimate the proportion of MYI and thick ice, given that new ice is introduced every year in the artificial holes.

5. Conclusions

In this study, we investigated the NSIDC sea ice drift data product using objective (frame independent) Eulerian and Lagrangian diagnostics. Results from this analysis complement previous studies documenting high random error (standard deviation) and systematic error (bias) in the NSIDC sea ice drift product, and identify one source for this systematic error: the direct assimilation of small-scale buoy velocity into the larger-scale ice drift velocity field inferred from satellites. Eulerian and Lagrangian diagnostics illustrate the resulting artificial divergence and stretching in the buoy-affected areas of the ice drift field. These artifacts, as demonstrated by Lagrangian metrics computed with a yearlong integration time, invalidate analysis of sea ice deformation that involves spatial gradients.

We have also used a simplified numerical model to show that age-of-ice calculations associated with sea ice motion and transport are also influenced by the existence of the above artifacts. Our numerical experiments specifically demonstrate loss of ice extent due to artificial divergence in buoy-affected regions. We have also highlighted the need for denser initial conditions than the evaluation grid to provide a more realistic representation of the number of floes, reducing artificial loss of ice extent.

Through a comparison of ice age model results [*Maslanik et al.*, 2011] with independent observations [*Comiso*, 2012] from 1983 to 2010, we have demonstrated the cumulative impact of artificial divergence. Numerical experiments illustrating correspondence between holes due to artificial divergence and difference in MYI extent between observed and modeled sea ice extent results support our findings. Our results show an underestimation of MYI extent, with an average value of 0.8×10^6 km^2 for the difference between model and measurement results in March. Such an underestimation of MYI extent will also have implications for sea ice thickness redistribution estimates.

Results from our Eulerian and Lagrangian analysis thus show that incorporation of raw buoy data using the MCC and cokriging techniques introduces artificial divergence/convergence features in the NSIDC ice drift product, which in turn undermines conclusions drawn from sea ice drift (ice age) and deformation (spatial gradients) studies based on these data.

Acknowledgments
The authors would like to thank the anonymous reviewers for their insightful comments and suggestions that have contributed to improve this paper. The authors thank the NSIDC and OSI SAF for providing sea ice motion data. NSIDC data are available for academic purposes through the NSIDC Portal (https://nsidc.org/data/docs/daac/nsidc0116_icemotion.gd.html or ftp://sidads.colorado.edu/pub/DATASETS/nsidc0116_icemotion_vectors_v3/data/north/week/). OSI SAF data are available for academic purposes through the OSI SAF Portal (ftp://osisaf.met.no/archive/ice/drift_lr/merged/). Thanks also to the Canada Research Chair (CRC) program and Natural Sciences and Engineering Research Council (NSERC) of Canada.

References

Arnold, V. I. (1978), *Mathematical Methods of Classical Mechanics*, Springer, New York.

Bouillon, S., and P. Rampal (2015), On producing sea ice deformation data sets from SAR-derived sea ice motion, *Cryosphere*, *9*, 663–673, doi:10.5194/tc-9-663-2015.

Comiso, J. (2012), Large decadal decline of the Arctic multiyear ice cover, *J. Clim.*, *25*(4), 1176–1193.

Comiso, J., and C. Hall (2014), Climate trends in the Arctic as observed from space, *5*, 389–409, doi:10.1002/wcc.277

Eicken, H., and A. R. Mahoney (2015), Sea ice: Hazards, risks and implications for disasters, in *Sea and Ocean Hazards, Risks and Disasters*, edited by J. T. Ellis, and D. J. Sherman, pp. 381–401, Elsevier, Oxford, U. K.

Fowler, C., W. Emery, and J. A. Maslanik (2003), Satellite derived arctic sea ice evolution October 1978 to March 2003, *IEEE Trans. Geosci. Remote Sens. Lett.*, *1*(2), 71–74.

Haller, G. (2001), Distinguished material surfaces and coherent structures in three-dimensional fluid flows, *Physica D*, *149*(4), 248–277, doi:10.1016/S0167-2789(00)00199-8.

Haller, G. (2015), Lagrangian coherent structures, *Annu. Rev. Fluid Mech.*, *47*, 137–162.

Hutchings, J. K., A. Roberts, C. Geiger, and J. Richter-Menge (2011), Spatial and temporal characterization of sea-ice deformation, *Ann. Glaciol.*, *52*(57 Pt 2), 360–368, doi:10.3189/2011AoG57A185.

Hutchings, J. K., and I. G. Rigor (2012), Role of ice dynamics in anomalous ice conditions in the Beaufort Sea during 2006 and 2007, *J. Geophys. Res.*, *117*, C00E04, doi:10.1029/2011JC007182.

Kimura, N., A. Nishimura, Y. Tanaka, and H. Yamaguchi (2013), Influence of winter sea ice motion on summer ice cover in the Arctic, *Polar Res.*, *32*, 2,0193, doi:10.3402/polar.v32i0.20.

Lavergne, T., S. Eastwood, Z. Teffah, H. Schyberg, and L.-A. Breivik (2010), Sea ice motion from low-resolution satellite sensors: An alternative method and its validation in the Arctic, *J. Geophys. Res.*, *115*, C10032, doi:10.1029/2009JC005958.

Marcq, S., and J. Weiss (2012), Influence of sea ice lead-width distribution on turbulent heat transfer between the ocean and the atmosphere, *Cryosphere*, *6*, 143–156.

Maslanik, J. A., C. Fowler, J. Stroeve, S. Drobit, J. Zwally, D. Yi, and W. Emery (2007), A younger, thinner Arctic ice cover: Increased potential for rapid, extensive sea-ice loss, *Geophys. Res. Lett.*, *34*, L24501, doi:10.1029/2007GL032043.

Maslanik, J., J. Stroeve, C. Fowler, and W. Emery (2011), Distribution and trends in Arctic sea ice age through spring 2011, *Geophys. Res. Lett.*, *38*, L13502, doi:10.1029/2011GL047735.

Rampal, P., J. Weiss, and D. Marsan (2009), Positive trend in the mean speed and deformation rate of Arctic sea ice, 1979–2007, *J. Geophys. Res.*, *114*, C05013, doi:10.1029/2008JC005066.

Rigor, I. G., and J. M. Wallace (2004), Variations in the age of Arctic sea ice and summer sea-ice extent, *Geophys. Res. Lett.*, *31*, L09401, doi:10.1029/2004GL019492.

Schwegmann, S., C. Haas, C. Fowler, and R. Gerdes (2011), A comparison of satellite-derived sea ice motion with drifting buoy data in the Weddell Sea, *Ann. Glaciol.*, *52*, 103–110.

Spreen, G., R. Kwok, and D. Menemenlis (2011), Trends in Arctic sea ice drift and role of wind forcing: 1992–2009, *Geophys. Res. Lett.*, *38*, L19501, doi:10.1029/2011GL048970.

Stroeve, J. C., J. A. Maslanik, M. C. Serreze, I. Rigor, W. Meier, and C. Fowler (2011), Sea ice response to an extreme negative phase of the Arctic Oscillation during winter 2009/2010, *Geophys. Res. Lett.*, *38*, L02502, doi:10.1029/2010GL045662.

Sumata, H., T. Lavergne, F. Girard-Ardhuin, N. Kimura, M. A. Tschudi, F. Kauker, M. Karcher, and R. Gerdes (2014), An intercomparison of Arctic ice drift products to deduce uncertainty estimates, *J. Geophys. Res. Oceans*, *119*, 4887–4921, doi:10.1002/2013JC009724.

Sumata, H., R. Kwok, R. Gerdes, F. Kauker, and M. Karcher (2015a), Uncertainty of Arctic summer ice drift assessed by high-resolution SAR data, *J. Geophys. Res. Oceans*, *120*, 5285–5301, doi:10.1002/2015JC010810.

Sumata, H., R. Gerdes, F. Kauker, and M. Karcher (2015b), Empirical error functions for monthly mean Arctic sea-ice drift, *J. Geophys. Res. Oceans*, *120*, 7450–7475, doi:10.1002/ 2015JC011151.

Tschudi, M., C. Fowler, J. Maslanik, and J. Stroeve (2010), Tracking the movement and changing surface characteristics of Arctic sea ice, *IEEE J. Sel. Top. Appl. Earth Obs. Remote Sens.*, *3*(4), 536–540.

Tschudi, M., C. Fowler, J. Maslanik, J. S. Stewart, and W. Meier (2016), *Polar Pathfinder Daily 25 km EASE-Grid Sea Ice Motion Vectors.Version 3. [indicate subset used]*, Natl. Snow and Ice Data Cent., Boulder, Colo., doi:10.5067/O57VAIT2AYYY, [Accessed April, 2016.]